PROCEEDINGS OF SPIE

SPIEDigitalLibrary.org/conference-proceedings-of-spie

Scattering field enhanced biosensing based on sub-wavelength split-ring plasmonic cavity with high Q-factor

Xiao Jin, Lu Xue, Jichuan Xiong, Shengwei Ye, Weiqing Cheng, et al.

Xiao Jin, Lu Xue, Jichuan Xiong, Shengwei Ye, Weiqing Cheng, Lianping Hou, John Marsh, Bin Ni, Bin Xu, Xuefeng Liu, "Scattering field enhanced biosensing based on sub-wavelength split-ring plasmonic cavity with high Q-factor," Proc. SPIE 12396, Plasmonics in Biology and Medicine XX, 1239607 (16 March 2023); doi: 10.1117/12.2647937

SPIE.

Event: SPIE BiOS, 2023, San Francisco, California, United States

Scattering Field Enhanced Biosensing Based on Sub-wavelength Split-ring Plasmonic Cavity with high Q-factor

Xiao Jin*[1], Lu Xue[1], Jichuan Xiong[1], Shengwei Ye[2], Weiqing Cheng[2], Lianping Hou[2], John Marsh[2], Bin Ni[1], Bin Xu[1], Xuefeng Liu[1]

[1]School of Electronic and Optical Engineering, Nanjing University of Science and Technology, Nanjing 210094, P. R. China

[2]James Watt School of Engineering, University of Glasgow, Glasgow, G12 8QQ, UK

*jinxiao@njust.edu.cn

ABSTRACT

Plasmonic structures are widely used in modern biosensor design. various plasmonic resonant cavities could efficiently achieve a high Q-factor, improving the local field intensity to enhance photoluminescence or SERS (Surface-Enhanced Raman Scattering) of small molecules. Also, the combination between virus-like particles and plasmonic structures could significantly influence the scattering spectrum and field, which is utilized as a method for biological particle detection. In this paper, we designed one kind of gold plasmonic cavity with the shape of a split-ring. An edge gap and a bonus center bulge are introduced in the split-ring structure. Our simulation is based on Finite Difference Time Domain (FDTD) method. Polarization Indirect Microscopic Imaging (PIMI) technique is used here to detect far-field mode distribution under the resonant wavelength. The simulation results demonstrate resonant peaks in the visible spectrum at about 600 nm with a Q-factor reaches to 74. Localized hot spots are generated by an edge dipole mode and a cavity hexapole mode at resonant wavelength, which is according to dark points in the PIMI sinδ image. Also, the split-ring cavity shows a sensitivity when combined with biological particles. The scattering distribution is evidently changed as a result of energy exchange between particles and split-ring cavity, indicating a promising possibility for biosensing.

Keywords: Plasmonic, Split-ring, PIMI, Biosensing

1. INTRODUCTION

The plasmonic excitation could be divided into surface plasmon resonances (SPR) and localized surface plasmon resonances (LSPR). SPR is guided modes propagating along flat planar or grating metal/dielectric interfaces, and LSPR is the harmonic oscillation of conduction electrons in metallic nanostructures under an outer electric field [1, 2]. In the last decades, plasmonic structures have been widely used for biosensing. Due to the high sensitivity of resonant wavelength for the refractive index (RI), one application of plasmonic structures is the sensing of environmental RI or biological layer with different RI, i.e., bulk sensitivities and surface sensitivities, respectively [3, 4]. Another type of application utilizes the surface enhanced process. Surface enhanced fluorescence (SEF) make advantage of the amplification of fluorescence at the localized hot spot [5-7]. Similar to SEF, surface enhanced Raman scattering (SERS) focuses on the signals of Raman scattering, where the signals could be enhanced by 10^3 – 10^6 times [8-10]. surface-enhanced infrared absorption (SEIRA) spectroscopy could also enhance infrared absorption by direct mid-IR excitation of molecules on metal structures [11].

However, most applications of plasmonic structures for sensing concentrate on the change of spectrum, either the reflection spectrum of the plasmonic structures or the scattering spectrum from detected bioparticles. Extensive spatial information is ignored in these methods. In this research, A split-ring Au cavity with a high Q-factor of 74 is designed for biosensing with a traditional bulk sensitivity of 600 nm/RIU. In addition, when bioparticles are captured by the cavity, localized energy would leak into the particle, which results in a spatial change of polarization state at a different site.

Plasmonics in Biology and Medicine XX, edited by Tuan Vo-Dinh, Ho-Pui A. Ho, Krishanu Ray
Proc. of SPIE Vol. 12396, 1239607 · © 2023 SPIE · 1605-7422 · doi: 10.1117/12.2647937

2. MATERIALS AND METHODS

2.1 Sample preparation

The structure is fabricated on a Si substrate. After a cleaning process, a 400 nm thick layer Polymethyl Methacrylate (PMMA) photoresist was spun on the surface of the silicon sample by controlling the spinning speed. Electron beam lithography (EBL) was used to define the patterns on the PMMA resist. After development, a 10 nm thick Ti layer and a 1900 nm thick Au layer were deposited. The 10 nm thick titanium is used to enhance the metal adhesion with the Si surface. After a standard lift-off process, the gold nanodot array was finally realized.

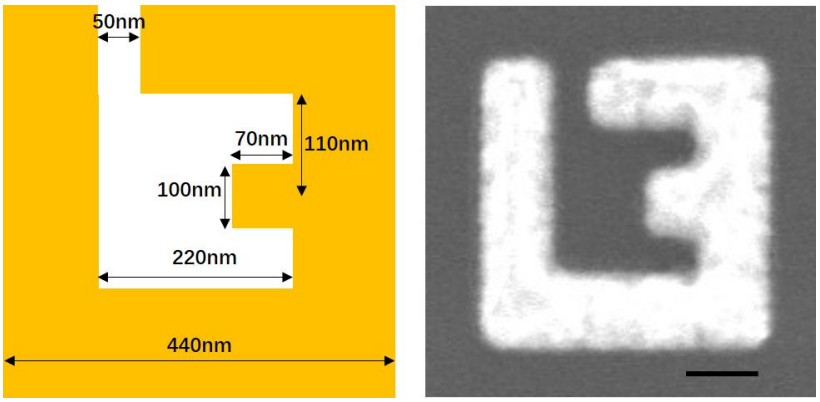

Figure 1. Sample configuration and the SEM result. Scale bar: 100 nm.

The detailed size parameters are shown in Fig 1. A fundamental rectangular ring structure is set with an outer width of 440 nm and an inner width of 220 nm. Then, a gap with a width of 50 nm split the ring structure at the edge of the inner rectangle. A bonus bulge with a size of 100 nm × 70 nm is placed at the transverse direction to generate an inner enhanced electric field and control the size of the particle the cavity captured.

2.2 Simulation setup and PIMI calculation

To analyze the near-field electromagnetic field and mode distribution, the simulation is implemented in a commercial software (Lumerical FDTD Solution). A plane wave source propagating along Z axis is set above the structure. the size of the periodic boundary is 600 nm along X and Y directions. When evaluating the polarization influence caused by a single bioparticle, a large period of 3000 nm is set in FDTD, and fabricated to avoid a field overlap between two adjacent units.

The calculation of the Q-factor followed a complementary harmonic inversion analysis method, which employs the filter diagonalization method to extract decay patterns in time series data [12, 13]. A time monitor is placed at the center point of the split-ring cavity for the calculation of the Q-factor. A sphere with a radius of 75 nm and a refractive index of 1.6 will be clipped inside the split-ring cavity to simulate the influence caused by bioparticles.

A polarization parameter imaging technique (PIMI, Polarized Indirect Microscopic Imaging) is utilized to detect the change of polarization state with a subwavelength resolution [14, 15]. The detecting process of PIMI system is shown in Fig 2.

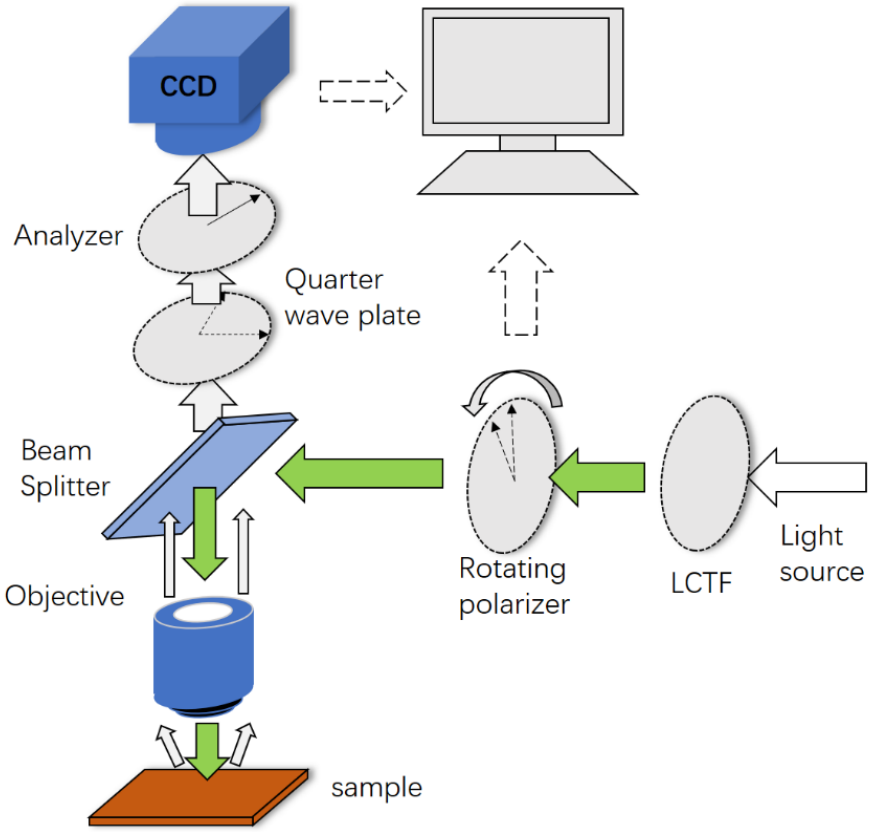

Figure 2. Diagram of PIMI measurement

After a polarization modulation for the monochromatic light source, the sample is illuminated under a 100X objective with NA = 0.9. The reflected light propagates through a 1/4 wave plate and a 45° polarizer, and is collected by a CCD (PiA2400-17gm, Basler). The output intensity could be expressed as

$$I_i = \frac{1}{2} I_0 \left[1 + \sin\delta \sin 2\left(\theta_i - \phi\right) \right]. \tag{1}$$

Here I_i (the subscript i indicates the number of polarization rotation angles) is the pixel intensity in each measured image. I_0 represents the average intensity under all illumination polarization states, which is also equivalent to the intensity obtained by a conventional microscope. $\sin\delta$ is the sine of the phase difference between two orthogonal polarization components of the scattered light. θ_i is the polarization angle of the linearly polarized incident beam and ϕ is the polarization ellipse orientation angle of the beam reflected from the sample. The same calculation is applied in FDTD, where a field monitor is placed at 300 nm height, to get the simulated PIMI results.

3. RESULTS AND DISCUSSION

In Fig 3, the background RI increases from 1.2 to 1.5 to evaluate the bulk sensitivity. Two narrow spectrum lines labeled by arrows occur when illuminated under either X or Y polarized light. The bulk sensitivity based on these lines is estimated at 600 nm/RIU, indicating a traditional biosensing application.

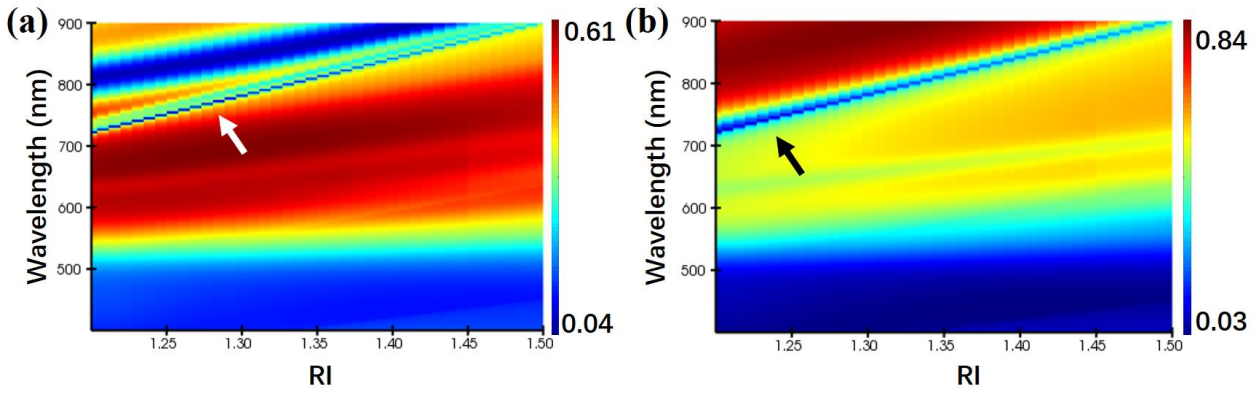

Figure 3. reflection spectrums of bulk sensitivity for illumination with (a) X and (b) Y polarization.

To clarify the sensing ability of bioparticles, it is necessary to analyze the interaction between particles and a single split-ring structure. As shown in Fig 4(a), a deep valley occurs at the wavelength of about 600 nm on the reflection spectrum under X polarization illumination, which represents a resonant peak. Based on the method in section 2.2, the Q-factor is calculated as 74 with a peak position at 608 nm. The appearance of the particle does not affect the shape of the reflection spectrum at 600 nm. In the bottom part of Fig 4(b), when the incident light oscillates along Y direction, another resonant peak appears at 602 nm with a Q-factor of 69. However, this resonant peak disappears when a particle is placed inside the cavity, showing a strong reaction between the split-ring structure and the bioparticle.

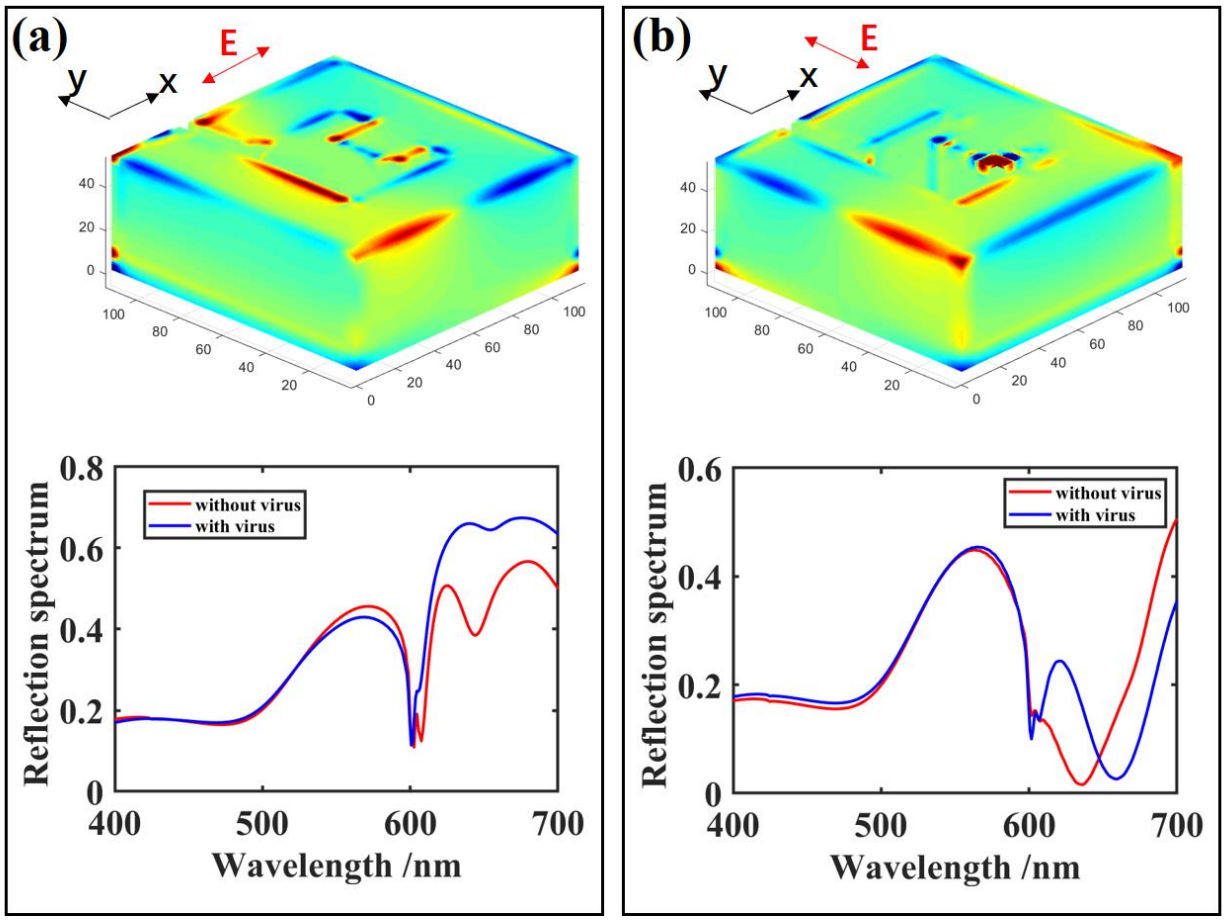

Figure 4. Surface charge distributions of the split-ring structure and reflection spectrums for illumination with (a) X and (b) Y polarization. Wavelength: 600 nm.

We also calculated the surface charge distributions for the split-ring structures under the resonant wavelength. In the upper part of Fig 4(a), a dipole mode is identified on the outer edge of the split-ring structure under X polarization. The dipole mode will also be split at two sides of gaps with two opposite charge oscillations. A similar dipole mode exists under Y polarization. Nevertheless, a localized hexapolar mode occurs on the surface of the bulge, indicating a possible enhancement of the electric field.

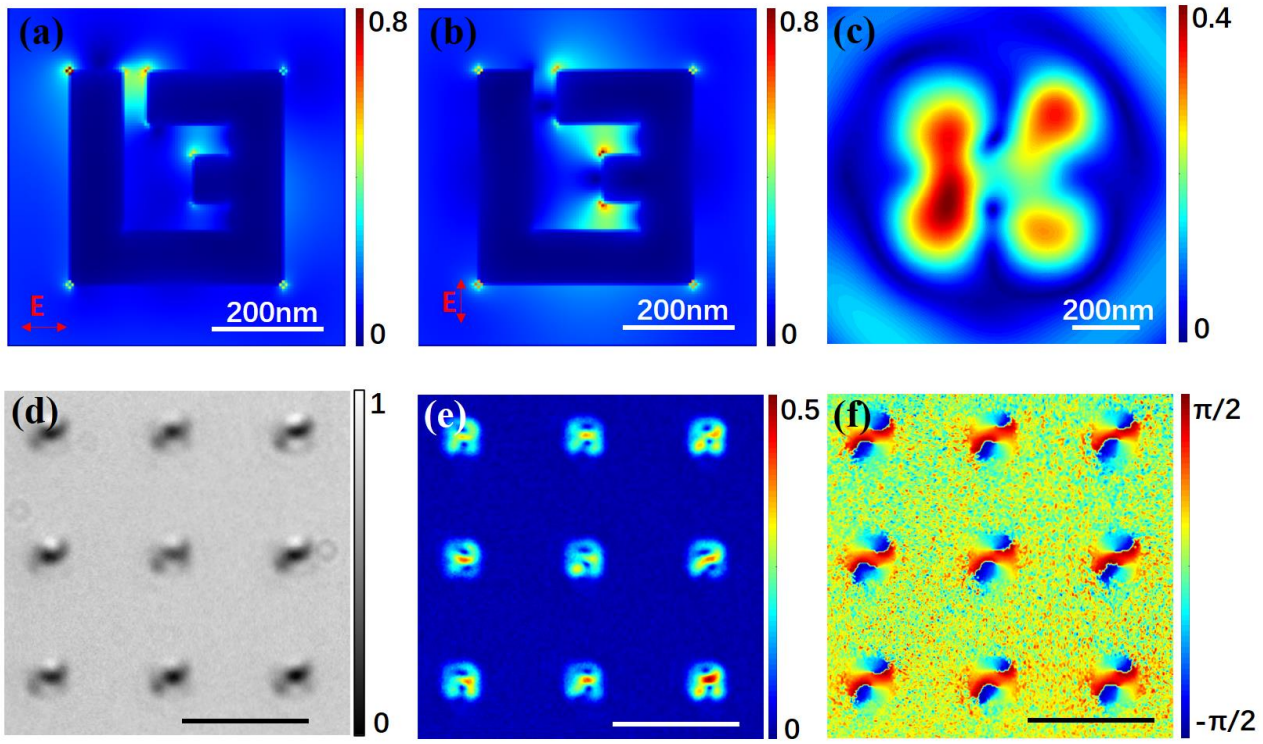

Figure 5. Electric field distributions for the split-ring without particle under (a) X polarization and (b) Y polarization. (c) PIMI sinδ image for the split-ring without particle. Images of split-ring structures from (d) traditional microscope, (e) PIMI sinδ parameter and (f) PIMI ϕ parameter. Scale bar: 3 μm.

The electric fields on the central cross-section under incident light with different orientations are shown in Fig 5(a) and (b). Under the transverse illumination, a hot spot is generated in the edge gap, related to the dipole mode. Corresponding to the hot spots inside the cavity in Fig. 5(b), the localized enhancement refers to the hexapole mode in Fig 4(b).

The simulated PIMI sinδ image is also shown in Fig 5(c). Two dark points are revealed in the image along the transverse direction, which represents the two hot spots of the hexapole mode. Due to the spatial distance of the hot spot of the dipole mode, the upper dark point possesses a displacement forward to the edge gap. A preliminary experimental result of PIMI images under 600 nm wavelength is shown in Fig 5(e) and (f). Similar to the simulation results, two dark points are shown in the transverse direction with a slight distance. In the ϕ image, these dark points correspond to phase singularity points.

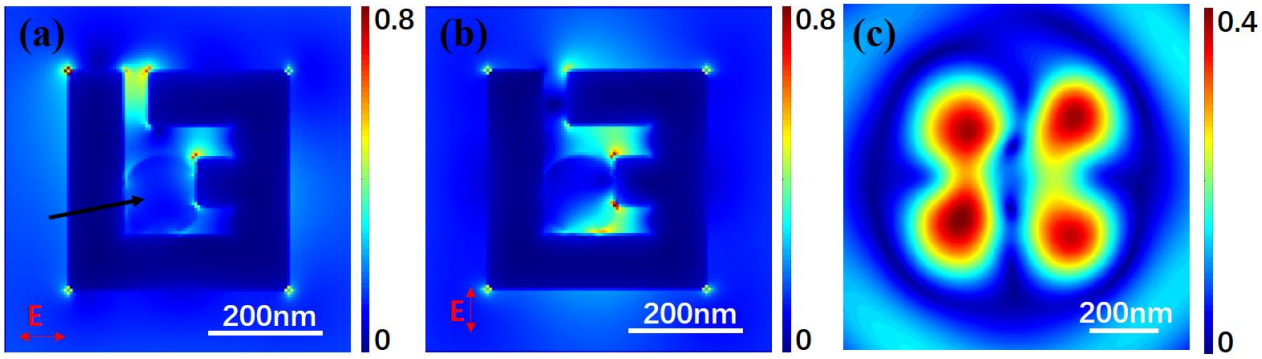

Figure 6. Electric field distributions for the split-ring with particle under (a) X polarization and (b) Y polarization. (c) PIMI sinδ image for the split-ring with a bioparticle.

The stable localized electric field will be broken when the bioparticle is added into the cavity. As Fig 6(a) and (b) indicate, the energy of hot spots leak into the bioparticle, which may transfer the near-field evanescent energy into propagable scattering field energy. Under the same simulation configuration, PIMI sinδ is simulated. We can clearly notice that two dark points merged into a line. Also, the left part is split into two hot points. These changes in the scattering distribution could be utilized as a judgment of the appearance of bioparticles.

4. CONCLUSION

In this article, a plasmonic split-ring structure array is designed for biosensing. As a traditional sensing application, this structure achieves a bulk sensitivity of 600 nm/RIU for the change of background refractive index. The resonant wavelengths of reflection spectrums exist at about 600 nm with Q- factor of 74 and 69 under X and Y polarized incident light, respectively. These resonant peaks correspond to a dipole mode occurring at the edge gap and an inner hexapole mode loaded by the bulge at the center of the split-ring. When the structure is used for sensing bioparticles, the captured bioparticle would break the mode distributions and transfer the near-field evanescent energy. In sinδ images, the two separated dark points therefore merge into a transverse line. We believe it shows a promising future for sensing various bioparticles.

REFERENCES

[1] Mejía-Salazar, J. R., Oliveira and Jr, O. N., "Plasmonic biosensing: Focus review," Chemical reviews, 118(20): 10617-10625 (2018).
[2] Unser, S., Bruzas, I., He, J., et al., "Localized surface plasmon resonance biosensing: current challenges and approaches," Sensors, 15(7), 15684-15716 (2015).
[3] Conteduca, D., Barth, I., Pitruzzello, G., et al., "Dielectric nanohole array metasurface for high-resolution near-field sensing and imaging," Nature communications, 12(1), 1-9 (2021).
[4] Xu, Y., Bai, P., Zhou, X., et al., "Optical refractive index sensors with plasmonic and photonic structures: promising and inconvenient truth," Advanced Optical Materials, 7(9), 1801433 (2019).
[5] Li, J. F., Li, C. Y. and Aroca, R. F., "Plasmon-enhanced fluorescence spectroscopy," Chemical Society Reviews, 46(13), 3962-3979 (2017).
[6] Jeong, Y., Kook, Y. M., Lee, K., et al., "Metal enhanced fluorescence (MEF) for biosensors: General approaches and a review of recent developments," Biosensors and Bioelectronics, 111, 102-116 (2018).
[7] Fort, E. and Grésillon, S., "Surface enhanced fluorescence," Journal of Physics D: Applied Physics, 41(1), 013001 (2007).
[8] Langer, J., Jimenez, de Aberasturi. D., Aizpurua, J., et al., "Present and future of surface-enhanced Raman scattering," ACS nano, 14(1), 28-117 (2019).

[9] Stiles, P. L., Dieringer, J. A., Shah, N. C., et al., “Surface-enhanced Raman spectroscopy,” Annu. Rev. Anal. Chem., 1, 601-626 (2008).
[10] Lindquist, N. C., de Albuquerque, C. D. L., Sobral-Filho, R. G., et al., “High-speed imaging of surface-enhanced Raman scattering fluctuations from individual nanoparticles,” Nature nanotechnology, 14(10), 981-987 (2019).
[11] Mueller, N. S., Pfitzner, E., Okamura, Y., et al., “Surface-enhanced Raman scattering and surface-enhanced infrared absorption by plasmon polaritons in three-dimensional nanoparticle supercrystals,” ACS nano, 15(3), 5523-5533 (2021).
[12] Mandelshtam, V. A. and Taylor, H. S., “Harmonic inversion of time signals and its applications,” The Journal of chemical physics, 107, 6756-6769 (1997).
[13] Hoblos, A., Suarez, M., Guichardaz, B., et al., “Revealing photonic symmetry-protected modes by the finite-difference-time-domain method,” Optics Letters, 45, 2103-2106 (2020).
[14] Jin, X., Zhang, H., Ni, B., et al., “Label-free sensing below the sub-diffraction limit of virus-like particles by wide-field photon state parametric imaging of a gold nanodot array,” Nanoscale Advances, 3, 6882-6887 (2021).
[15] Jin, X., Ye, S., Cheng, W., Hou, J., Jin, W., Sheng, T., Hou, L., Marsh, J., Yu, Y., Sun, M., Ni, B., Liu, X. and Xiong, J., “Sub-wavelength visualization of near-field scattering mode of plasmonic nano-cavity in the far-field,” Nanophotonics. (2023).